applied sciences

MDPI

Article

Combustion and Performance Evaluation of a Spark Ignition Engine Operating with Acetone–Butanol–Ethanol and Hydroxy

Wilson Guillin-Estrada [1], Daniel Maestre-Cambronel [2], Antonio Bula-Silvera [1], Arturo Gonzalez-Quiroga [1] and Jorge Duarte-Forero [2,*]

[1] UREMA Research Unit, Universidad del Norte, Km. 5 Vía Puerto Colombia, Puerto Colombia, Barranquilla 080007, Colombia; wguillin@uninorte.edu.co (W.G.-E.); abula@uninorte.edu.co (A.B.-S.); arturoq@uninorte.edu.co (A.G.-Q.)

[2] KAÍ Research Unit, Universidad del Atlántico, Carrera 30 Número 8-49, Puerto Colombia, Barranquilla 080007, Colombia; dmaestre@est.uniatlantico.edu.co

* Correspondence: jorgeduarte@mail.uniatlantico.edu.co; Tel.: +57-5385-3002

Abstract: Alternative fuels for internal combustion engines (ICE) emerge as a promising solution for a more sustainable operation. This work assesses combustion and performance of the dual-fuel operation in the spark ignition (SI) engine that simultaneously integrates acetone–butanol–ethanol (ABE) and hydroxy (HHO) doping. The study evaluates four fuel blends that combine ABE 5, ABE 10, and an HHO volumetric flow rate of 0.4 LPM. The standalone gasoline operation served as the baseline for comparison. We constructed an experimental test bench to assess operation conditions, fuel mode, and emissions characteristics of a 3.5 kW-YAMAHA engine coupled to an alkaline electrolyzer. The study proposes thermodynamic and combustion models to evaluate the performance of the dual-fuel operation based on in-cylinder pressure, heat release rate, combustion temperature, fuel properties, energy distribution, and emissions levels. Results indicate that ABE in the fuel blends reduces in-cylinder pressure by 10–15% compared to the baseline fuel. In contrast, HHO boosted in-cylinder pressure up to 20%. The heat release rate and combustion temperature follow the same trend, corroborating that oxygen enrichment enhances gasoline combustion. The standalone ABE operation raises fuel consumption by around 10–25 g • kWh^{-1} compared to gasoline depending on the load, whereas HHO decreases fuel consumption by around 25%. The dual-fuel operation shows potential for mitigating CO, HC, and smoke emissions, although NOx emissions increased. The implementation of dual-fuel operation in SI engines represents a valuable tool for controlling emissions and reducing fuel consumption while maintaining combustion performance and thermal efficiency.

Keywords: acetone–butanol–ethanol; dual-fuel operation; electrolyzer; emissions levels; hydroxy gas; spark ignition engine

Citation: Guillin-Estrada, W.; Maestre-Cambronel, D.; Bula-Silvera, A.; Gonzalez-Quiroga, A.; Duarte-Forero, J. Combustion and Performance Evaluation of a Spark Ignition Engine Operating with Acetone–Butanol–Ethanol and Hydroxy. *Appl. Sci.* **2021**, *11*, 5282. https://doi.org/10.3390/app11115282

Academic Editors: Cinzia Tornatore and Luca Marchitto

Received: 31 March 2021
Accepted: 7 May 2021
Published: 7 June 2021

1. Introduction

The escalation of the world population and the unprecedented trend of energy consumption represent significant challenges of the current century. The massive utilization of internal combustion engines (ICE) has led to worldwide modernization while supporting the current living standards; however, such high-scale utilization has also resulted in uncontrolled fossil fuel consumption and alarming environmental pollution [1–3]. The latter represents a complex problem since ICEs play a central role in different sectors such as transportation, agriculture, power generation, and industry, thus setting intensified pressure on pollution deceleration [4–6]. Governmental and international organizations have made a tremendous effort to potentialize global energy transition to renewables while simultaneously setting restrictions in various sectors to mitigate the rate of greenhouse emissions [7,8].

The transition to alternative fuels in both compression ignited (CI) and spark-ignited (SI) engines is a pressing need, which emerges as a feasible solution to promote a more reliable operation, minimize global emissions and reduce fossil-fuel dependence. The investigation around CI engines is extensive and diverse as more than 144 biodiesel blends have been reported in the literature with promising results for a reliable and cleaner operation [9].

In the same way, the implementation of alternative fuels in SI engines has been broadly discussed. In this scenario, there is an inclined trend towards implementing oxygenated compounds such as bioethanol and biobutanol. Biobutanol offers different advantages as it can be blended in gasoline at relatively high mixing ratios without modifying the engine functionality. However, the main drawback of biobutanol is the high energy consumption associated with its production, which is based on the acetone–butanol–ethanol (ABE) fermentation process. Therefore, the direct implementation of ABE is a more reliable option from a techno-economic viewpoint. The utilization of ABE and other alcohol additives in SI engines has already been documented in the literature.

For instance, Masum et al. [10] investigated the influence on overall emissions and combustion performance of partial fuel substitution in SI engines with oxygenated fuels such as methanol, butanol, and pentanol in a volumetric replacement of 20%. The engine torque was maximized by using all the fuel blends, whereas emissions levels were minimized moderately. Similarly, Yacoub et al. [11] experimentally evaluated the overall performance of mixing gasoline with different straight-chain alcohol chains from methanol to pentanol (C1–C5) in a SI engine. This study unravels the importance of achieving optimal operating conditions within the engine to guarantee CO and HC emissions minimization. In contrast, the NOx emissions presented both upward or downward trends depending on the engine operating conditions. Nithyanandan et al. [12] examined the overall performance of ABE solution in different volumetric ratios, namely 3:6:1, 6:3:1, and 5:14:1. The study outlines the predominant role of increasing acetone content (6:3:1) as the brake thermal efficiency is improved since the combustion phasing resembles that of pure gasoline.

In the same vein, different perspectives in ethanol implementation have been derived from promoting sustainable operation in ICEs. Di Blasio et al. [13] implemented advanced optical methodologies to analyze the main structural and chemical characteristics of soot particles emitted by ethanol-fueled engines. The results demonstrated the low incidence of ethanol incorporation on the quality and nanostructure of soot emissions. Likewise, Gargiulo et al. [14] outlined that ethanol fumigation positively impacts the greenhouse emissions levels while reducing the concentration of emitted particles. Beatrice et al. [15] revealed the central role of engine calibration, pilot injection, and rail pressure to optimize the benefits of ethanol towards emissions minimization and higher thermal efficiency in CI engines. Similarly, Vassallo et al. [16] allocated the pressing need for research on advanced injection systems as a concrete driver of CO_2 emissions targets in the future state of ICEs while maintaining high power density. Belgiorno et al. [17] elaborated on recent advances that integrate gasoline partially premixed combustion in Euro 5 diesel engines. The study focused on describing the effects of appropriate calibration parameters, pilot quantity, and exhaust gas recirculation to maximize thermal efficiency and reduce global pollutants.

On the other hand, hydrogen technology gradually becomes a prominent candidate as an energy carrier that can promote an enhanced operation in both CI and SI engines based on environmental and operational perspectives. Hydrogen production is primarily led by gas reforming technologies representing nearly 60% of the global production [18]. Nonetheless, the carbon footprint of reforming-based production schemes features several challenges to contribute to greenhouse emissions minimization. Therefore, the role of hydrogen production via water-splitting and biomass technologies will be of increased interest in the mid-long term of the hydrogen market [19]. The continuous research on electrolyzers has facilitated the construction of sophisticated and feasible components that maintain proper operation, high-purity reactant agents, and reasonable production rates [18–20].

Therefore, since water electrolysis produces hydrogen and oxygen, the gaseous fuel enrichment in ICEs can be performed either with standalone hydrogen operation and hydroxy gas (HHO).

Shivaprasad et al. [21] experimentally evaluate the influence of hydrogen doping from 5% to 25% in a single-cylinder. Increasing hydrogen replacement increases the in-cylinder pressure while minimizing both HC and CO emissions; however, the adverse effect of such implementation was the intensification of NOx formation. Ismail et al. [22] envisioned HHO enrichment as a secondary fuel in SI engines encountering promising results towards enhancing thermal efficiency and power output and decreasing emissions. Yilmaz et al. [23] revealed that a constant volumetric HHO enrichment in the engine triggers adverse effects in power output, fuel consumption, and emissions levels. Therefore, the authors implemented a hydroxy control unit to control the volumetric rates of gaseous fuel replacement via voltage and current variations to guarantee the optimal rate based on the engine operation. In this way, they managed to reduce fuel metrics, overall emissions and enhance thermal performance.

The main contribution of this investigation is to evaluate the performance of the dual-fuel operation in spark ignition (SI) engines while simultaneously implementing hydroxy (HHO) gas enrichment and acetone–butanol–ethanol (ABE) as additive. The study incorporates evaluation metrics based on combustion performance, thermal efficiency, fuel consumption, and emissions levels. The novelty of this paper relies on the incorporation of a complete methodology to predict combustion performance and energy/exergy distributions. This study examines a combined fuel operation mode in SI, which has not drawn sufficient attention in published studies. In the development of the experimental assessment, ABE is used in different volumetric ratios, namely 5% (ABE 5) and 10% (ABE 10), whereas hydroxy gas is implemented as gaseous fuel in volumetric flow additions of 0.4 LPM. Moreover, the study includes a complete characterization of the experimental test bench, hydroxy generation system, instrumentation, and measuring uncertainty. Therefore, this work represents a further effort on closing the knowledge gap in the implementation of alternative fuels in SI engines while pinpointing experimental and numerical guidelines to evaluate the performance of dual-fuel technologies.

This paper is structured as follows: Section 2 outlines the main features of the experimental test bench, tested fuels, instrumentation characteristics, and describes the constitutive formulation of the combustion and thermodynamic modeling. Section 3 provides the core findings while critically discussing the outcomes. Finally, Section 4 states the concluding remarks while describing the limitations and future avenues in the field.

2. Materials and Methods

2.1. Experimental Test Bench

The experiments were performed in a 4T, naturally aspirated spark-ignition engine (model MZ175, YAMAHA®). The engine has a volumetric capacity of 171 cm^3 and a compression ratio of 8.5:1. It is worth discussing the relevance of the volumetric capacity in ICEs since it provides a clear perspective of the context of the present application. In essence, this matter is essential, considering that international and governmental regulations concerning greenhouse emissions in the transportation sector are based on the volumetric capacity. The typical taxation margin is classified as low (<1000 cc), middle (1200–1500 cc), and high (>1500 cc) capacity [24]. Note that the engine used in this study is intended for power generation applications. However, its operational characteristics resemble those in commercial vehicles, extending the impact spectrum of the proposed dual-fuel technology. Table 1 lists the main features of the SI engine.

Table 1. Specifications of the gasoline engine.

Specification	Value
Engine type	4T OHV
Max. Power	3.5 kW
Bore × Stroke	66 × 50 mm
Max. Torque	10.5 Nm/2400 rpm
Compression ratio	8.5:1
Fuel capacity	4.5 L
Ignition system	T.C.I
Displacement	171 cc

A picture of the test bench is shown in Figure 1. The experimental setup consists of the SI engine, hydroxy generation system, and DAQ system, as shown in Figure 2. Firstly, the SI engine is integrated into a dynamometer to control the load condition. A crankshaft angle sensor (Beck Arnley 180–042) allows measuring engine speed. The in-cylinder pressure is measured with a piezoelectric transducer (KISTLER type 7063-A) placed in the cylinder head. The engine fuel consumption rate is obtained via a scale (OHAUS PA313) and a chronometer. On the other hand, intake airflow is measured employing a hot-wire type mass sensor (BOSCH 22,680 7J600). Additionally, the temperatures of the exhaust gases were measured using K-type thermocouples. Lastly, the measurement of CO, NOx, and HC emissions was carried out using two different gas analyzers, namely BrainBee AGS-688 and PCA® 400. An additional gas analyzer (BrainBee OPA-100) measured the opacity levels of the exhaust gases. The measuring instruments were integrated into a data acquisition system that processes the output data. Table 2 lists the main features of the measuring instruments of the test bench.

Figure 1. Experimental test bench.

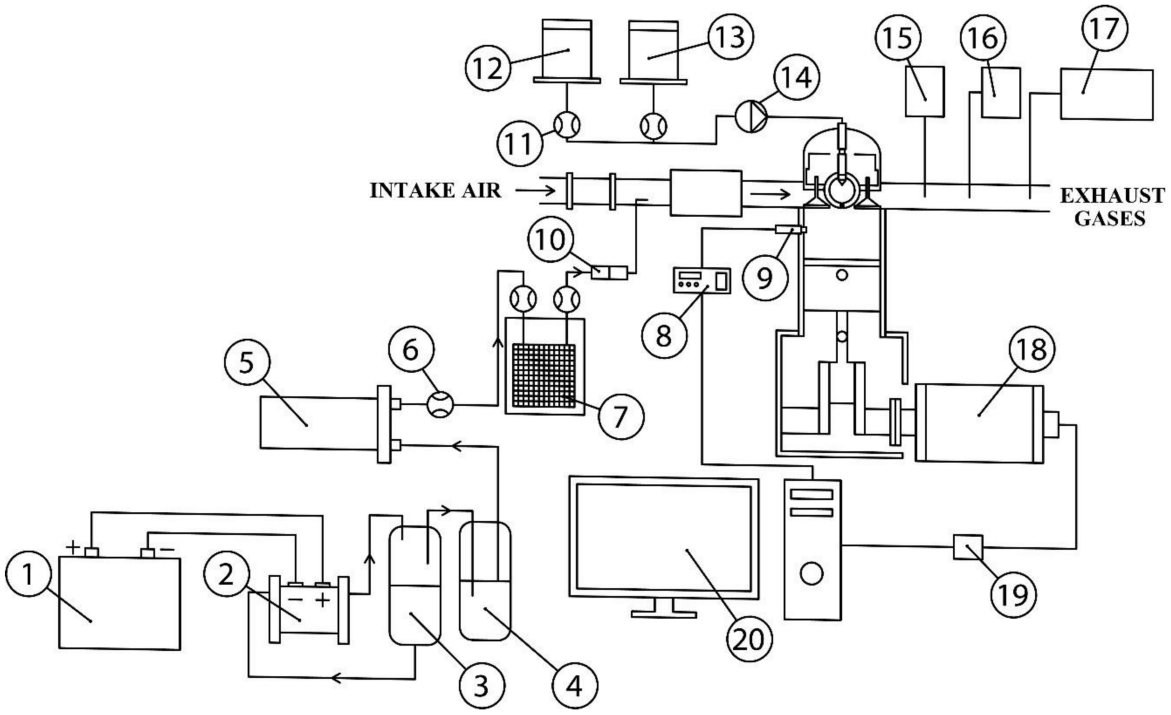

Figure 2. Schematic representation of the experimental test bench. (1) AC-DC converter; (2) electrolyzer cell; (3) electrolytic tank; (4) bubbler; (5) HHO storage tank; (6) HHO flowmeter; (7) flame arrester; (8) charge amplifier; (9) pressure sensor; (10) silica gel filter; (11) flowmeter; (12) gasoline tank; (13) ABE tank; (14) fuel pump; (15) BrainBee AGS-688 emission gas; (16) PCA 400 emission gas analyzer; (17) opacimeter BrainBee OPA-100; (18) alternator; (19) encoder; (20) data acquisition (DAQ) system.

Table 2. Specifications of measuring instruments.

Parameter	Instrument	Manufacturer	Range
Cylinder pressure	Piezoelectric transducer	KISTLER type 7063-A	0–250 bar
Airflow	Air mass sensor	BOSCH OE-22680 7J600	0–125 g/s
Angle	Crankshaft angle	Beck Arnley 180–0420	5–9999 RPM
Fuel measuring	Gravimetric meter	OHAUS-PA313	0–310 g
HHO gas flow	HHO flow rate	GT-556-MTR-ICV	0–3 LPM
Temperature	Temperature sensor	Type K	−200–1370 °C
CO	Exhaust gas analyzer	BrainBee AGS-688	0–9.99%
HC			0–9999 ppm
NOx		PCA-400	0–3000 ppm
Smoke opacity		BrainBee OPA-100	0–99.9%

The hydroxy gas addition was carried out by means of an HHO gas generator installed in the engine intake system (see Figure 2). Hydroxy gas is obtained through a dry cell made of stainless steel, with the ability to withstand high temperatures and currents. Additionally, this type of material does not cause a chemical reaction with the electrolytic substance. To improve cell performance, KOH was used as a catalyst at a concentration of 20% (gram of solute/volume of solution). This allows improving the conductivity of the dry cell.

An electrolytic tank constantly supplies a flow of water to the dry cell to maintain constant hydroxy production. Additionally, a bubbler tank was installed to retain the water content in the hydroxy gas. Two flame arresters and a silica gel filter were installed to prevent flashback.

The measurement uncertainty results from various factors such as measuring instrumentation, calibration, and external environmental conditions [25]. The type A evaluation method, which comprises the statistical evaluation of a series of measurements, was employed. The type A method calculates the best estimate (b_i) of a set of measurements (x_1, x_2, x_3, ... x_n) using Equation (1):

$$b_i = \overline{x} = \frac{1}{n} \bullet \sum_{i=1}^{n} x_i \quad (1)$$

In the uncertainty model, the standard deviation (S) assists in calculating the error dispersion of a set of measurements (x_1, x_2, x_3, ... x_n) as expressed in Equation (2).

$$S = \sqrt{\frac{1}{n-1} \bullet \sum_{i=1}^{n} (x_i - \overline{x})^2} \quad (2)$$

Lastly, the model uses the standard uncertainty to measure the mean experimental standard deviation $u(x_i)$ from the measurements.

$$(x_i) = \frac{1}{\sqrt{n}} \bullet \sqrt{\frac{1}{n-1} \bullet \sum_{i=1}^{n} (x_i - \overline{x})^2} \quad (3)$$

where n refers to the number of repetitions in the measurements.

Our study set a total of five repetitions ($n = 5$) in the experiments for each operational variable following previous studies [26]. Table 3 shows the uncertainty associated with each operational variable.

Table 3. Measurement uncertainty of measured variables.

Variable	Uncertainty (%)
Pressure chamber	±0.4
Air mass	±1.2
Crankshaft angle	±1.1
Gravimetric meter	±1.2
HHO flow rate	±1.0
CO_2	±1.1
HC	±1.5
Smoke opacity	±2.0
NOx	±1.5
Total uncertainty	±3.8

2.2. Tested Conditions and Fuel Characteristics

Table 4 lists the properties of the gasoline and the ABE blend oxygenates. Here we implemented ABE additive in a mixing ratio of 3:6:1, which has been implemented in SI engines [27].

The study also used two different alcohol blends, namely ABE 5 and ABE 10, representing the replacement rate in gasoline fuel. Table 5 shows the main properties of these blends.

Table 4. Properties of the fuels used in this study [28].

Parameter	Units	Gasoline	Acetone	Butanol	Ethanol
Chemical formula	-	$C_4 - C_{12}$	C_3H_6O	C_4H_9OH	C_2H_5OH
LHV	$(MJ \bullet kg^{-1})$	43.4	29.6	33.1	26.8
Density	$(kg \bullet m^{-3})$	737	788	810	789
Vaporization latent heat	$(kJ \bullet kg^{-1})$	440	518	716	904
Autoignition temperature	(°C)	300	465	343	420
Laminar flame speed	$(cm \bullet s^{-1})$	33	34	48	39

Table 5. Properties of the ABE blends.

Parameter	Units	ABE5	ABE10
LHV	$(MJ \bullet kg^{-1})$	42.79	42.20
Density	$(kg \bullet m^{-3})$	740.38	743.76
Latent Vaporization heat	$(kJ \bullet kg^{-1})$	451.77	463.54
Autoignition temperature	(°C)	304.36	308.73
Laminar flame velocity	$(cm \bullet s^{-1})$	33.49	33.99

On the other hand, hydroxy doping has been implemented directly in the intake air system, and the volumetric flow replacement follows the methodology proposed by Ismail et al. [29]. The latter states that a suitable gas substitution rate is 0.25 LPM for an engine capacity of 1000 cm^3. Therefore, this study used a 0.04 LPM replacement rate. The main properties of the hydroxy gas that serves within the modeling are: density $(0.49\ kg \bullet m^{-3})$ and the LHV $(21.99\ MJ \bullet kg^{-1})$. The experimental assessment alternates the dual-fuel operation in the engine to relate the influence of hydroxy and ABE compounds. A series of 15 runs were established, as shown in Table 6.

Table 6. Nomenclature and composition of fuels.

Test	RPM	Load (%)	Fuel Mixture Composition	Symbology
1	2400	50	100% Gasoline	G
2			95% Gasoline + 5% ABE	ABE5
3			90% Gasoline + 10% ABE	ABE10
4			95% Gasoline + 5% ABE + 0.04 LPM Hydroxy	ABE5 + HHO
5			90% Gasoline + 10% ABE + 0.04 LPM Hydroxy	ABE10 + HHO
6		75	100% Gasoline	G
7			95% Gasoline + 5% ABE	ABE5
8			90% Gasoline + 10% ABE	ABE10
9			95% Gasoline + 5% ABE + 0.04 LPM Hydroxy	ABE5 + HHO
10			90% Gasoline + 10% ABE + 0.04 LPM Hydroxy	ABE10 + HHO
11		100	100% Gasoline	G
12			95% Gasoline + 5% ABE	ABE5
13			90% Gasoline + 10% ABE	ABE10
14			95% Gasoline + 5% ABE + 0.04 LPM Hydroxy	ABE5 + HHO
15			90% Gasoline + 10% ABE + 0.04 LPM Hydroxy	ABE10 + HHO

2.3. Fundamentals of the Combustion and Thermodynamic Models

The fundamental formulation implemented in this paper represents a simplified model of the physical phenomena due to required modeling assumptions. First, all combustion gases in all stages follow ideal gas behavior [30]. Moreover, the flame propagation speed is considered to operate below the supersonic condition, assuming a uniform pressure in the combustion chamber [31]. The combustion reactants are assumed in stoichiometric amounts, considering that a significant part of the combustion results from diffusion

interactions. Similarly, reactant's properties are calculated using an average temperature in the combustion chamber, which entails thermal stabilization as a result of the diffusion process. Finally, the model accounts for heat exchange interactions in the cylinder liner to reinforce the model prediction capabilities.

As a first insight, the model establishes the first law of thermodynamics for an open system, which constitutes the combustion chamber. In essence, this model enables the characterization of the heat release curves as a function of the engine operating conditions. Accordingly, Equation (4) gives an energy balance for the control volume neglecting macroscopic effects [32]:

$$\frac{dU}{d\theta} = \frac{dQ}{d\theta} - \frac{dW}{d\theta} + \sum_i \frac{dH_i}{d\theta} \tag{4}$$

where U refers to internal energy, Q and W represent heat and mechanical work, respectively. H refers to the system enthalpy, and θ relates to the crank angle.

The heat release rate (H_{RR}) can be expressed as defined in Equation (5):

$$H_{RR} = \frac{m_{comb} \bullet C_v \bullet \frac{dT}{d\theta} + P \bullet \frac{dV}{d\theta} + R \bullet T \bullet \frac{dm_{bb}}{d\theta} + \frac{dQ_r}{d\theta} - \frac{dm_{fuel}}{d\theta} \bullet (h - u)}{m_{comb} \bullet LHV} \tag{5}$$

where m_{comb},m_{fuel}, and m_{bb} refer to the mass of combustion gases, fuel, and blow-by gas, respectively. Additionally, R, h, u, V, and T represent the ideal gas constant, specific enthalpy, specific internal energy, volume, and temperature, respectively, which are parameters that assist in determining the thermodynamic state of the fuel mixture. Lastly, Q_r , C_v, and LHV refer to rejected heat, specific heat at constant volume, and lower heating value, respectively.

2.3.1. Calculation of Combustion Gases Properties

Firstly, the average temperature inside the combustion chamber is calculated via Equation (6), which includes the universal gas constant (R). The latter is calculated via Equation (7).

$$T = \frac{P \bullet V}{m_{comb} \bullet R} \tag{6}$$

$$R = X_{air} \bullet R_{air} + X_{st} \bullet R_{st} + X_g \bullet R_g \tag{7}$$

where R_{air}, R_{st} and R_g refer to the air gas constants of air, stoichiometric combustion, and gaseous fuel, respectively. Similarly, X_{air}, X_{st} and X_g correspond to the mass fraction of the gases mentioned above.

On the other hand, the specific heat ratio of combustion gases uses the Zucrow and Hoffman correlation [33], as described in Equation (8).

$$\gamma(T) = 1.46 - 1.63 \bullet 10^{-4} \bullet T + 4.14 \bullet 10^{-8} \bullet T^2 \tag{8}$$

Subsequently, the specific heat at constant volume of the combustion gases is given by Equation (9):

$$C_v(T) = \frac{R}{\gamma(T) - 1} \tag{9}$$

Lastly, both the specific enthalpy and internal energy are calculated as a function of the specific heat ratio, which is temperature-dependent, as shown in Equations (10) and (11), respectively.

$$h(T) = R \int \frac{\gamma(T)}{\gamma(T) - 1} \, dT \tag{10}$$

$$u(T) = R \int \frac{1}{\gamma(T) - 1} \, dT \tag{11}$$

2.3.2. Blow-by Gas Losses

As previously discussed, the blow-by gas losses phenomena account for a significant share of energy losses. Therefore, incorporating such effects in the thermodynamic model becomes a determinant factor in predicting the operating conditions [34]. Hence, the study implements the formulation introduced by Irimescu [35] to predict the energy losses derived from exhaust gas leakage inside the combustion chamber as described in Equations (12) and (13).

$$\frac{dm_{bb}}{d\theta} = \frac{P_{ext} \bullet A_v \bullet C_D}{N \bullet (R \bullet T_{ext})^{1/2}} \bullet \left(\frac{P_{int}}{P_{ext}}\right)^{1/\gamma(T)} \bullet \left[2 \bullet \frac{\gamma(T)}{\gamma(T)-1} \bullet \left(1 - \left(\frac{P_{int}}{P_{ext}}\right)^{\frac{\gamma(T)-1}{\gamma(T)}}\right)\right]^{1/2} \tag{12}$$

$$\frac{dm_{bb}}{d\theta} = \frac{P_s \bullet A_v \bullet C_D}{\gamma(T)^{1/2} \bullet N \bullet (R \bullet T_{ext})^{1/2} \bullet \left[1 - \left(\frac{2}{\gamma(T)+1}\right)^{\frac{\gamma(T)+1}{2 \bullet (\gamma(T)-1)}}\right]}$$

$$if, \frac{P_{int}}{P_{ext}} \leq \left(\frac{2}{\gamma(T)-1}\right)^{\frac{\gamma(T)-1}{\gamma(T)}} \tag{13}$$

where P_{ext} and P_{int} represent the exhaust and intake flow pressures, respectively. N refers to the engine speed. C_D and A_v account for the discharge coefficient and engine valve area calculated via Equations (14) and (15), respectively.

$$C_D = \frac{\dot{m}_{fuel}}{\dot{m}_t} \tag{14}$$

$$A_v = \frac{\pi \bullet {D_v}^2}{4} \tag{15}$$

where $\dot{m}_{fuel}$ is the experimental mass flow of the inlet valve and $\dot{m}_t$ is the theoretical mass flow rate, calculated considering a constant compressible flow through a valve orifice. Besides, D_v is the diameter of the valve and amounts to 28 mm.

2.3.3. Rejected Heat

The thermodynamic model used Equation (16) to predict the heat transfer rate from the combustion gases to the combustion chamber walls.

$$\frac{dQ_r}{d\theta} = \frac{h_{wall} \bullet A_{wall} \bullet (T - T_{wall})}{2 \bullet \pi \bullet N} \tag{16}$$

where T_{wall} and A_{wall} are the temperature and the wall surface area. Besides, h_{wall} is the heat transfer coefficient, calculated via the correlation proposed by Woschni [36] as given by Equation (17):

$$h_{wall} = 3.26 \bullet (w \bullet P)^{0.8} \bullet T^{-0.55} \bullet b^{-0.2} \tag{17}$$

where b accounts for the internal diameter of the combustion chamber and w represents the average velocity of the combustion gases. The latter is calculated via Equation (18).

$$w = k_1 \bullet (2 \bullet N \bullet S_t) + k_2 \bullet \frac{T_o \bullet V_d \bullet (P - P_m)}{P_o \bullet V_o} \tag{18}$$

Subscript "o" relates the initial state for volume (V_o), pressure (P_o) and temperature (T_o). P and P_m are the actual and mean pressure in the combustion chamber. k_1 and k_2 are model constants, whose values are defined as 2.30 and 3.25×10^{-3}, respectively. Finally, S_t represents the engine stroke.

2.3.4. Combustion Chamber Volume

Here we define the combustion chamber volumetric characteristics, which involve different volume contributions that incorporate operational and geometrical patterns to define the instantaneous volumetric displacement within each cycle [37]. Equation (19) gives the instantaneous volume of the combustion chamber.

$$V = V_{mv} + V_{disp} + \bullet V_{dp} + \bullet V_{inf} + \bullet V_c \tag{19}$$

The term V_{mv}, calculated via Equation (20), represents the free space encountered once the piston reaches the top-dead center (TDC).

$$V_{mv} = \frac{\pi \bullet D^2}{4} \bullet \left[\frac{2 \bullet L_{cr}}{r_c - 1}\right] \tag{20}$$

where r_c and D are the compression ratio and the internal diameter of the piston, respectively. L_{cr} represents crankshaft length and V_{disp} the volume displaced by the connecting rod-crank mechanism. The latter is predicted using Equation (21).

$$V_{disp} = \frac{\pi \bullet D^2}{4} \bullet \left[L_{cr} + L_{rod} - R_y \bullet \theta\right] \tag{21}$$

L_{rod} is the longitude of the crankshaft and R_y represents the vertical position of the piston. Consequently, the volumes denoted as ΔV_{dp} and ΔV_{inf} are calculated using Equations (22) and (23), respectively. The former represents the variation of the instantaneous volume induced by pressure-deformation effects imposed by the combustion gases. The latter accounts for the volume related to the inertial forces of the connecting rod-crank shaft mechanism.

$$\Delta V_{dp} = \frac{\pi \bullet D^2 \bullet L_{rod}}{4 \bullet A_c} \bullet \left(\frac{k_{def}}{E_s}\right) \bullet \left(P \bullet A_p\right) \tag{22}$$

$$\Delta V_{inf} = \frac{\pi \bullet D^2 \bullet L_{rod}}{4 \bullet A_c} \bullet \left(\frac{k_{def}}{E_s}\right) \bullet \left(m \bullet a_p\right) \tag{23}$$

where k_{def}, E_s, A_c, A_p and a_p are the deformation constant, the elastic modulus of steel, connecting rod critical area, the piston cross-sectional area, and piston acceleration, respectively.

Finally, ΔV_c is calculated according to Equation (24) and represents the variation of the instantaneous volume produced by the clearances in the combustion chamber [37].

$$\Delta V_c = -\frac{\pi \bullet D^2}{4} \bullet \sum_{i=1}^{2} (e_i \bullet \sin \varphi_i \bullet \cos \alpha_i) \tag{24}$$

where e represents the eccentricity between journal and bearing, measured along their centerline. Similarly, φ relates to the angle of rotation, and α represents the angle between the connecting rod and the piston.

2.3.5. Energy Distribution and Emissions Processing

The engine inlet heat energy ($\dot{Q}_{int}$) is defined based on the fuel mode, which can be entirely liquid using pure gasoline or oxygenated fuel blends with ABE as indicated in Equation (25), or alternately liquid-gaseous fuel, which constitutes the dual-fuel operation mode given by Equation (26).

$$\dot{Q}_{int} = \dot{m}_{fuel} \bullet LHV_f \tag{25}$$

$$\dot{Q}_{int} = \dot{m}_{fuel} \bullet LHV_{fuel} + \dot{m}_{HHO} \bullet LHV_{HHO} \tag{26}$$

where the subscripts fuel refers to the fuel mixture and HHO represents the hydroxy gas. Similarly, the model defines the exhaust gas energy as follows:

$$\dot{Q}_{exh} = \dot{m}_{exh} \bullet C_{p,exh} \bullet T_{exh} \tag{27}$$

where $C_{p,exh}$ represents the specific heat capacity of the combustion gases at constant pressure. On the other hand, the mechanical efficiency of the engine according to the fuel mode is defined as follows.

Liquid fuel standalone operation:

$$\eta_{mech} = \frac{PW}{\dot{m}_{fuel} \bullet LHV_{fuel}} \bullet 100 \tag{28}$$

Dual-fuel mode:

$$\eta_{mech} = \frac{PW}{\dot{m}_{fuel} \bullet LHV_{fuel} + \dot{m}_{HHO} \bullet LHV_{HHO}} \bullet 100 \tag{29}$$

where PW is the power output of the engine calculated according to Equation (30).

$$PW = \frac{2 \bullet \pi \bullet \omega \bullet T_r}{60 \bullet 1000} \tag{30}$$

where T_r is the torque condition, and ω refers to the engine angular speed. Lastly, this section concludes with the calculation of the unit conversion of the overall emissions.

On the other hand, the measuring instrumentation for emissions levels is commonly reported in ppm and %vol, which are the default characteristics of gas analyzers. However, it is necessary to apply further processing to display these results according to the international standards (i.e. European legislation) that describe pollutants in terms of g $\bullet$ km^{-1} for light-dutty and passenger vehicles and g $\bullet$ kWh^{-1} for heavy-duty vehicles [38]. Therefore, the study converts the output data from the gas analyzers into g $\bullet$ kWh^{-1} according to the empirical correlations proposed by Heseding and Daskalopoulos [39]. The relevance of the emissions above processing is that they assist in relating emissions and fuel metrics, facilitating comparison. The correlation for emissions processing is based on the following formulation:

$$EP_i = EV_{i,dry} \bullet \left(\frac{M_i}{M_{exh,dry}} \bullet k_d \right) = EV_{i,wet} \bullet \left(\frac{M_i}{M_{exh,wet}} \bullet k_w \right) \tag{31}$$

where EP_i, $EV_{i,dry}$ and $EV_{i,wet}$ represents the pollutant mass in the power unit (g $\bullet$ kWh^{-1}), exhaust emissions on a dry basis and wet basis, respectively. The term M_i accounts for the molecular mass, while $M_{exh,d}$ and $M_{exh,w}$ relates to the molecular mass of exhaust emissions on a dry and wet basis, respectively. Finally, the terms k_{dry} and k_{wet} are empirical constants with a value of 3.873 g $\bullet$ kWh^{-1} and 4.160 g $\bullet$ kWh^{-1}, respectively, and relate the power unit and the exhaust emissions on a dry basis and wet basis, respectively. The conversion of the three primary pollutants treated in experimental evaluation is described in Equation (32) to (34) [39].

$$CO \left[\frac{g}{kWh} \right] = 3.591 \bullet 10^{-3} \bullet CO(\%\, vol) \tag{32}$$

$$NOx \left[\frac{g}{kWh} \right] = 6.636 \bullet 10^{-3} \bullet NOx(ppm) \tag{33}$$

$$HC \left[\frac{g}{kWh} \right] = 2.002 \bullet 10^{-3} \bullet HC(ppm) \tag{34}$$

3. Results and Discussion

3.1. Cylinder Pressure

The experimental evaluation of the dual-fuel operation in the SI engine begins with the characterization of the pressure gradients developed within the combustion chamber. This parameter provides a clear perspective of the fuel mode performance while relating the appropriate mixing interaction between the base fuel (gasoline/ABE), hydroxy gas (gaseous fuel), and air. Figure 3 shows the overall behavior of the in-cylinder pressure at different load conditions. Notice that the standalone gasoline operation has been set as the baseline fuel for comparison purposes.

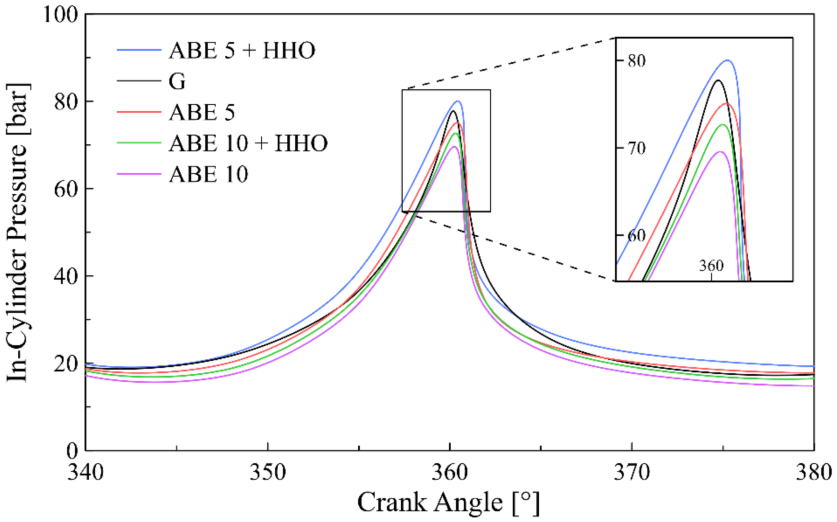

(**a**)

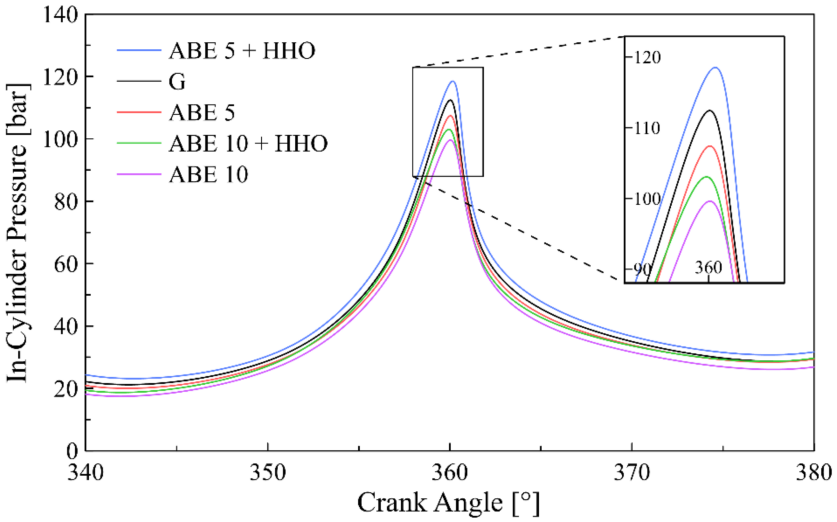

(**b**)

Figure 3. *Cont.*

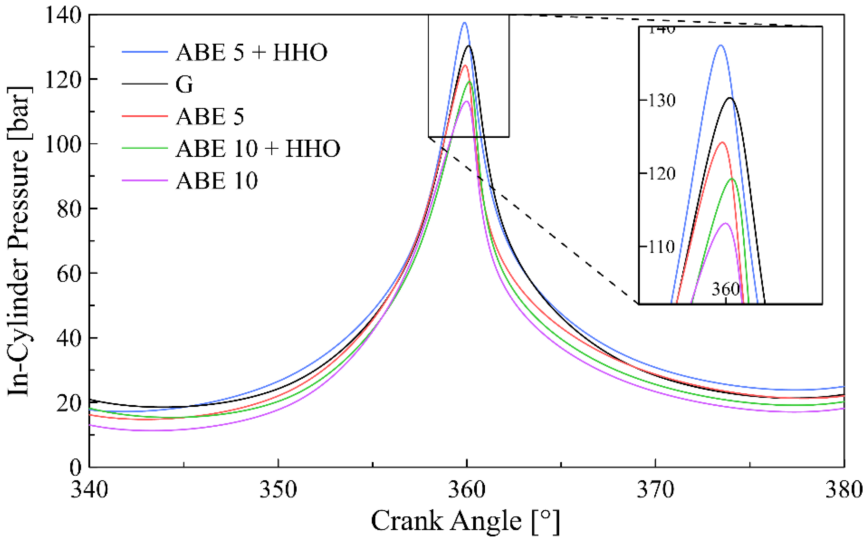

(**c**)

Figure 3. Influence of fuel on cylinder pressure for an engine load of (**a**) 50%, (**b**) 75%, and (**c**) 100%.

According to the results, the maximum in-cylinder pressure within the engine operating range is achieved by the ABE 5 + HHO with values between 60–135 bar. This result is consistent with the magnification of the laminar flame speed of this blend. Results in Figure 3 assist in the evaluation of the combustion phasing from the different fuel blends. Based on Figure 3a, all the blends present a retarded phasing between 0.2°–0.6° compared to the baseline fuel, which implies that a low engine load inhibits the fast combustion for the alternative fuels. The overall pattern encountered in the phasing is consistent with related investigations of ABE at different blend ratios [12]. Next, in Figure 3b, all the tested fuels feature a relatively similar phasing condition. However, at high engine loads (Figure 3c), the enhancement on the laminar flame speed from the oxygenated fuels becomes evident as the combustion phasing is advanced, ranging from 0.8° to 1.6° compared to the baseline, which facilitates the completion of combustion and faster peak pressures achievement even before reaching 360°. The latter is a direct indication of a significant improvement in combustion efficiency and thermal performance.

The pressure curve features an increasing trend as the engine load increases since more fuel is mixed to meet the power demand. Notably, increasing the fuel substitution with ABE (ABE 10) limited the pressure produced during combustion between 30–70 bar, which can be associated with the lower calorific value of this blend. This result agrees with similar investigations related to diesel engine combustion phenomena while operating with biodiesel blends [40]. Another contributor to the reduced pressure of ABE-based blends could be associated with a higher-octane rating that extends the initiation delay and reduces the laminar flame speed. In contrast, hydroxy doping enables a significant improvement in the combustion pressure in both blends (ABE 5/10) up to 75%. This pattern can be explained considering that incorporating hydroxy in the engine facilitates a homogeneous air-fuel mixture. The positive effects on the gasoline octane rating by incorporating HHO in the intake air system can be mentioned as another contributor to the enhanced combustion performance since the compression ratio is maximized. It should be noted that the overall trend of the pressure curves after combustion features a sharp decrement which guarantees that the knocking condition is not reached. On average, the combustion pressure developed in the standalone gasoline operation is higher than that of ABE 5, ABE 10, and ABE 10 + HHO by 12%, 18%, and 24%, respectively. Contrarily, the ABE 5 + HHO shows an enhanced pressure range compared to commercial gasoline between 10–15% for the engine load ranges analyzed.

3.2. Heat Release Rate (H_{RR})

The H_{RR} relates to the fuel conversion efficiency since it shows how much chemical energy is transformed into thermal energy. Figure 4 depicts the H_{RR} at different engine load conditions as a function of the crankshaft angle.

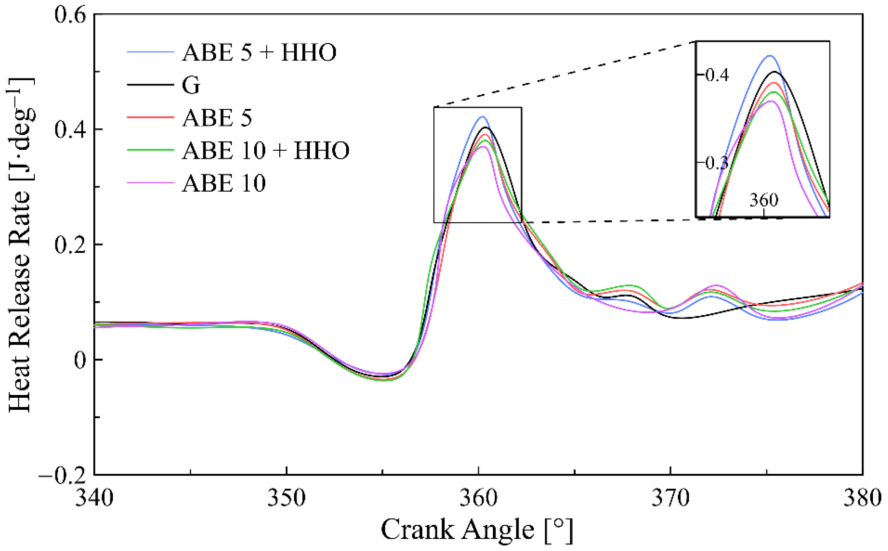

(**a**)

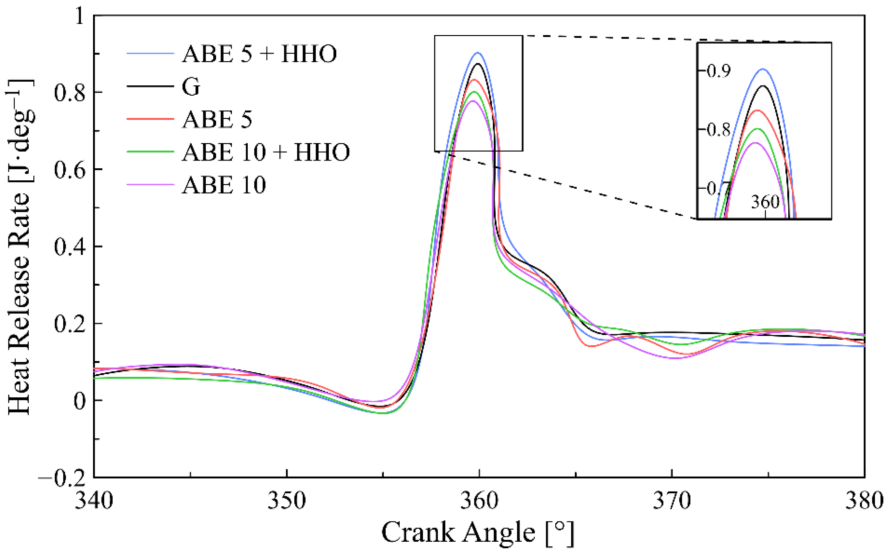

(**b**)

Figure 4. *Cont.*

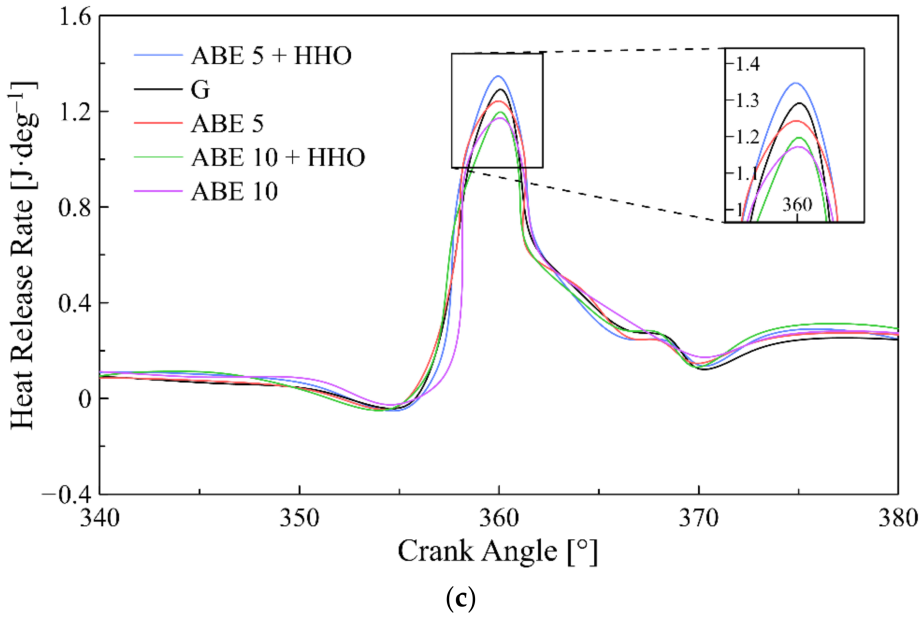

(**c**)

Figure 4. Influence of fuel on heat release rate for (**a**) 50%, (**b**) 75%, (**c**) 100% of the engine load.

According to the results, the general pattern in all the load conditions states that ABE 5 + HHO features the highest heat release from the fuel blends, followed by gasoline, ABE 5, ABE 10 + HHO, and ABE 10. It can be observed that a higher engine load promotes the increase of heat release in the combustion chamber, which implies extreme conditions and maximum chemical energy conversion. The average reduction of the H_{RR} for the ABE 5 and ABE 10 was 3.5% and 6.78%, respectively, compared to gasoline as the baseline fuel. The latter can be explained considering the higher viscosity of these blends that promote a slower combustion process, thus limiting heat release.

HHO enrichment increases heat release in all the blends, which implies integrating gaseous fuel mitigates the cooling effect associated with utilizing oxygenates (ABE). The higher calorific value and subsequent enhancement in the laminar flame speed resulting from HHO doping can be mentioned as contributors to the enhanced behavior in the heat release that offset the decrement experienced by ABE blends when compared to pure gasoline. It is worth mentioning that the fuel chemical structure supports the enhanced behavior from HHO doping since both hydrogen and oxygen coexist in the air/fuel mixture, whereas gasoline consists of hydrocarbon molecules [41]. Therefore, the gaseous fuel incorporation promotes an improved combustion performance due to the direct interaction of the diatomic molecules that suppress the ignition delay. In this sense, HHO doping also fosters the massive bond-breaking trend of the gasoline molecules, thus facilitating the heat release rate, the laminar flame speed, and subsequently improving combustion efficiency.

3.3. Combustion Chamber Temperature

Figure 5 shows the average temperature of the combustion chamber for the tested fuels. This parameter indicates the ability of a blend for combustion phasing. Notice that the study only presents the temperature distribution for a full load rate, representing the critical condition from the analyzed cases since it holds the highest heat release rate and maximum pressure peaks.

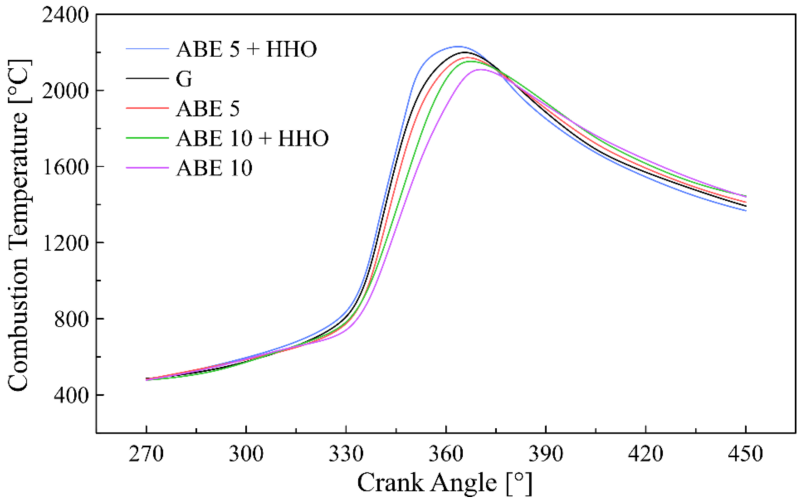

Figure 5. In-cylinder temperature at a full load rate.

According to the results, the maximum temperature is achieved by ABE 5 + HHO, followed by the gasoline, ABE 5, ABE 10 + HHO, and ABE 10. Interestingly, the temperature after combustion presents a reverse trend concerning the blends, which can be associated with the higher heat release rate during combustion, minimizing the temperature in this stage. The maximum temperature reaches a value of 2229 °C for ABE 5 + HHO, supporting the energetic contribution derived from the dual-fuel operation. Moreover, as the ABE content escalates, the combustion temperature drops between 20–45%. This pattern can be explained considering the lower heating value and intensified latent heat of the ABE blends. Notably, increasing the latent heat promotes a temperature drop in the intake stage, resulting in a lower temperature at the end of the compression stage. Moreover, incorporating hydroxy gas in the blends intensifies the temperature due to the higher hydrogen and oxygen content that stimulates the chemical energy conversion of the air/fuel mixture [42]. On average, the combustion chamber temperature of ABE 5 and ABE 10 decreased by 6.21% and 12.23% compared to the gasoline fuel. In contrast, HHO enrichment increases the temperature of ABE 5 and ABE 10 by up to 394 °C and 341 °C, respectively.

3.4. Engine Performance

The study points out the brake specific fuel consumption (BSFC) overall trend in Figure 6 that is driven to examine the fuel mass consumption per power unit while providing a global perspective of this parameter.

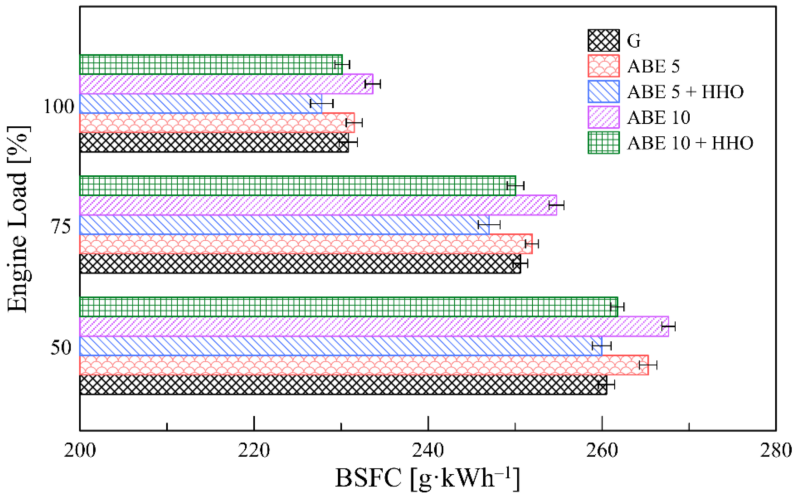

Figure 6. Diagram of Brake Specific Fuel Consumption (BSFC).

According to the results, the implementation of oxygenated blends (ABE 5 and ABE 10) promotes higher fuel consumption when compared to the standalone gasoline operation. The latter is a direct consequence of the lower energy density and lower calorific value relative to gasoline. Therefore, a higher fuel amount is required to obtain the same unit power, which escalates the BSFC. For comparison, increasing the ABE ratio fosters the BSFC up to 15%. This pattern is in line with other investigations [12,43]. Note that the ABE-based blends might influence the octane rating rise, supported by longer ignition delays (Figure 4c) that critically limits the power output, thus magnifying BSFC. The fuel conversion efficiency might be a determinant factor altering the fuel metrics since it was corroborated in the in-cylinder pressure curves that at low engine loads, the combustion center retarded up to 0.6°. Therefore, the altered combustion phasing further deteriorates fuel conversion efficiency, thus increasing fuel consumption. The investigation of Nithyanandan [12] leads to similar findings when implementing blends of ABE 20–40. In this sense, the integration of control strategies that facilitates spark timing could be a feasible solution to avoid the magnification of BSFC in dual-fuel operation [44,45].

The highest fuel consumption was achieved by ABE 10, followed by the ABE 5, Gasoline, ABE 10 + HHO, and ABE 5 + HHO. This result demonstrates that HHO enrichment surpasses the increment in the fuel metrics derived from ABE replacement implementation. The latter implies that gaseous fuel promotes chemical conversion efficiency while acting as a heat intensifier, as verified in Figure 5.

3.5. Emission Characteristics

This section aims to examine the influence of dual-fuel operation on the overall emissions of the SI engine. Reducing greenhouse emissions facilitates an eco-friendly operation in the ICEs. The study mainly examines the pollutant levels of CO, HC, NOx, and smoke opacity while variating fuel operation mode and the engine load.

3.5.1. CO Emissions

First, the overall carbon monoxide emissions (CO) for all the tested fuels are displayed in Figure 7 at different load conditions.

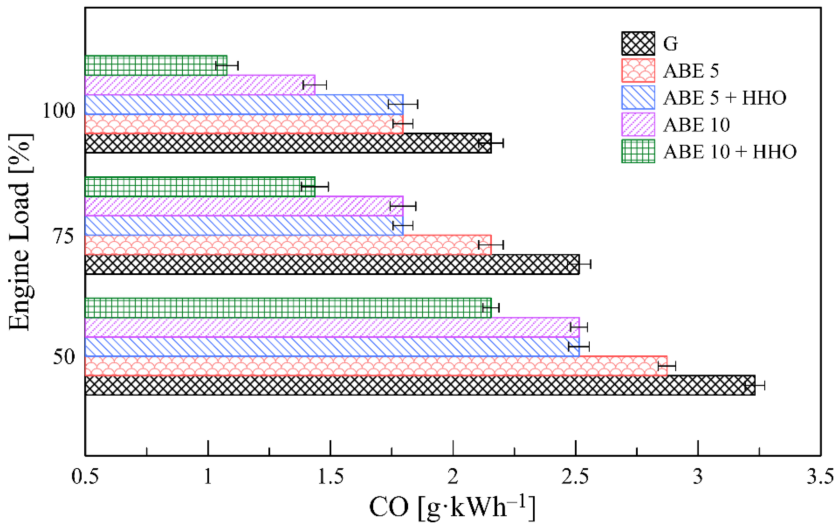

Figure 7. CO emissions for fuels tested.

The load condition features an inverse relation with the CO emission levels. The engine load plays a central role in the emissions behavior since, at high engine loads, it can be reached a non-oxygenated condition that promotes CO formation. However, the high CO formation remains high at low engine loads due to a highly lean mixture that hinders fuel burning. Thus, the flame cannot be maintained due to the limited propagation speed.

Specifically, the ABE implementation reduces CO emissions between 11% to 33% compared to gasoline, depending on the engine load. The HHO implementation enables a further reduction of up to 22%. The enhanced behavior from the fuel blends results from promoting complete combustion, meaning that more CO is converted into CO_2. Additionally, the ABE incorporation facilitates oxidation due to the increased laminar flame speed and the leaning effect of its oxygenated nature. The higher volatility derived from the acetone in the ABE blends further promotes CO minimization. Li et al. [46] encountered that the ABE features a post-flame oxidation trend that reduces CO levels.

The implementation of HHO doping in the intake air minimizes CO levels, which can also be explained considering the direct oxygen enrichment in the air/fuel mixture. CO emission is directly linked to the air/fuel ratio within the engine and the fuel consumption. Hence, since hydroxy enrichment reduces the BSFC (Figure 6), fewer CO levels are evidenced in the exhaust gases.

It is worth underlying the trade-off of the proposed fuel methodology since the CO minimization resulted in intensified CO_2 formation. Considering that international regulations claimed for integral solutions to meet CO_2 standards, it triggers a collateral cost impact in the proposed dual-fuel technology due to the imminent necessity to engage additional methods to promote a sustainable operation in future scenarios. Di Blasio et al. [13] have pointed out the predominant role of advanced fuel injection systems in this goal. Moreover, the latter technology is accompanied by additional improvements in fuel economy and combustion noise that reinforce its implementation. Undoubtedly, implementing such sophisticated fuel injection systems increases the investment cost that can be only supported by substantial fuel savings while maintaining high-efficiency operation. Moreover, considering the effect of combustion phasing, the necessity to control spark timing to promote higher combustion efficiencies requires in-depth exploration of engine design characteristics and fuel injection systems that foster a techno-economic operation.

3.5.2. HC Emissions

Figure 8 shows the overall emissions of hydrocarbons (HC) as a function of the engine load.

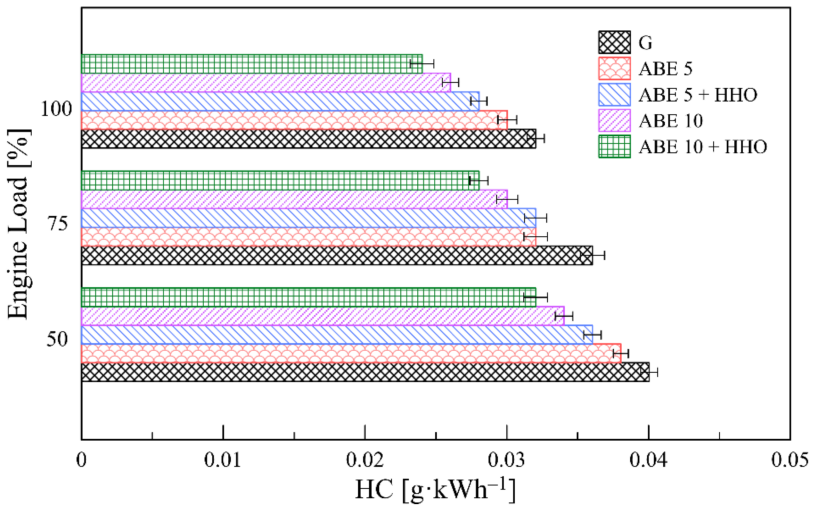

Figure 8. HC emissions for fuels tested.

In terms of unburned hydrocarbons, pure gasoline features the highest emissions levels with nearly 0.042 g • kWh^{-1}. Dual-fuel operation facilitates HC minimization since ABE reduces emissions levels while hydroxy doping upgrades this share. Noticeably, HC emissions are significantly lower than CO levels but still represents an undesired pollutant that affects human health and air quality. The overall trend of HC emissions can be explained based on the same fundamentals of CO emissions. It is important to note that

alcohols additives (ABE) feature improved oxygenated characteristics that further improve combustion efficiency and promote a homogeneous air/fuel mixture, which reduces HC formation. These concluding remarks are consistent with that of Masum et al. [10], which unravels the effect of engine speed on ABE blend overall performance. The enhanced laminar flame speed of ABE and HHO is another contributor supporting HC minimization.

3.5.3. NOx Emissions

Figure 9 shows NOx formation for all the tested fuels as a function of engine load. The increment in combustion temperature sets the appropriate conditions to promote nitrogenates oxidation, thus producing NOx. Therefore, it can be stated that NOx formation depends significantly on the in-cylinder temperature, the concentration of oxygen in the fuel, and the residence time of the reaction.

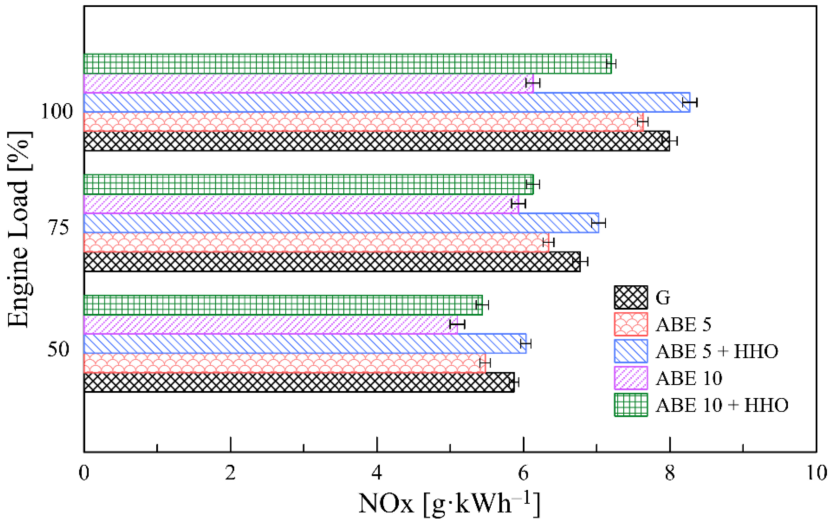

Figure 9. NOx emissions for fuels tested.

Based on the results, the maximum NOx emissions are reached at a full engine load. Specifically, ABE implementation facilitates reducing the overall emissions of NOx, but HHO upgrades this share. The latter implies that the magnification of the in-cylinder temperature provided by the hydroxy doping suppresses the positive effect of the ABE. The enhanced behavior of ABE standalone blends can be attributed to the higher vaporization heat that limits the air-fuel mixture temperature in the intake stage, which reflects on reduced combustion temperature, thus reducing the potential of NOx formation. This pattern is consistent with the experimental outcome of a similar investigation that directly measures the temperature at the intake valve closing [12,46].

The highest NOx emission levels were achieved by the ABE 5 + HHO, followed by pure gasoline, ABE 5, ABE 10 + HHO, and ABE 10. Incorporating the oxygenated compounds in the air/fuel mixture reduces NOx emissions between 0.36 to 1.87 g • kWh^{-1} compared to gasoline. In contrast, the integration of hydroxy doping in the intake air for the ABE 5 case maximizes the emissions levels between 0.16 to 0.27 g • kWh^{-1} but ABE 10 + HHO remains behind the baseline fuel during all the engine loads. The higher oxygen content in the air/fuel mixture can directly contribute to the rise in NOx emissions by incorporating HHO in the fuel blends.

It is essential to mention the trade-off between the effect of HHO doping based on fuel economy and emission levels. Based on the fuel metrics (Figure 6), the integration of hydroxy gas minimizes fuel consumption, which ratifies prospective benefits in terms of fossil-fuel depletion and economic viewpoints. Moreover, since ABE is replacing up to 10% of fossil fuel, the net fuel saving escalates based on a global perspective. In the counterpart, hydroxy doping stimulates NOx formation, as corroborated in this section. A potential solution to mitigate the impact of NOx emissions magnification could be integrating waste

heat recovery (WHR) technologies that further enable a higher fuel utilization ratio. The integration of exhaust gas recirculation systems can be another feasible opportunity to promote the sustainable operation of ICEs.

3.5.4. Smoke Emissions

The emissions section concludes with the smoke opacity emission depicted in Figure 10 for the different tested fuels.

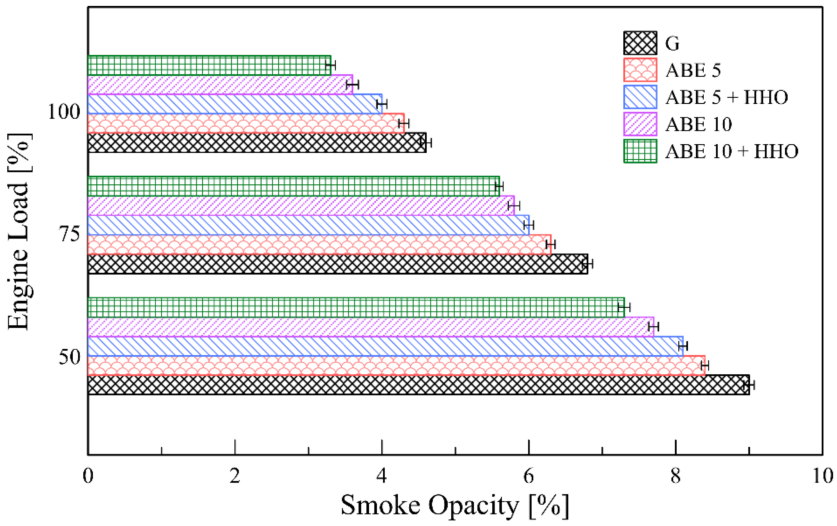

Figure 10. Smoke emission for fuels tested.

According to the results, the emissions levels of smoke opacity are higher at low engine loads. In this sense, as the engine load increases from 50% to 100%, the emissions are reduced up to 54%, demonstrating that smoke emissions depend primarily on the engine operating conditions. Interestingly, the standalone gasoline operation features the highest smoke formation in the exhaust stream. On the contrary, implementing alcohol compounds and HHO doping promotes smoke opacity minimization. This result implies that the extension of the oxygenated conditions limits the emission levels. In other words, it is observed that by only using ABE additive in the blends, a decent reduction of smoke is achieved when compared to the baseline fuel, and the HHO replacement furthers enlarge the smoke drop. Specifically, gasoline presents up to 9% of smoke emissions, followed by ABE 5 between 4.2 to 8.3% and ABE 10 with less than 7.6%. The implementation of hydroxy enrichment in ABE 5 and ABE 10 provides a further reduction of up to 0.3% and 0.4%, respectively.

Exhaust after-treatment technologies have reported salient results towards emissions reduction. However, the main advantage of the proposed dual-fuel methodology relies on the simplified implementation that does not intervene in engine structure and requires negligible modification on its functionality. The latter elucidate clear advantages from a techno-economic viewpoint and the importance of promoting dual-fuel operation in future platforms of ICEs.

3.5.5. Fuel Energy Distribution

This section concludes by examining the fuel energy distribution within the engine for the tested fuels. Accordingly, Figure 11 summarizes the fuel energy allocation based on the power output and exhaust gases directly measured on the experimental assessment. Notice that the energy loss comprises lubrication oil, refrigerant, among other energy losses such as blow-by gas that limit energy conversion [34].

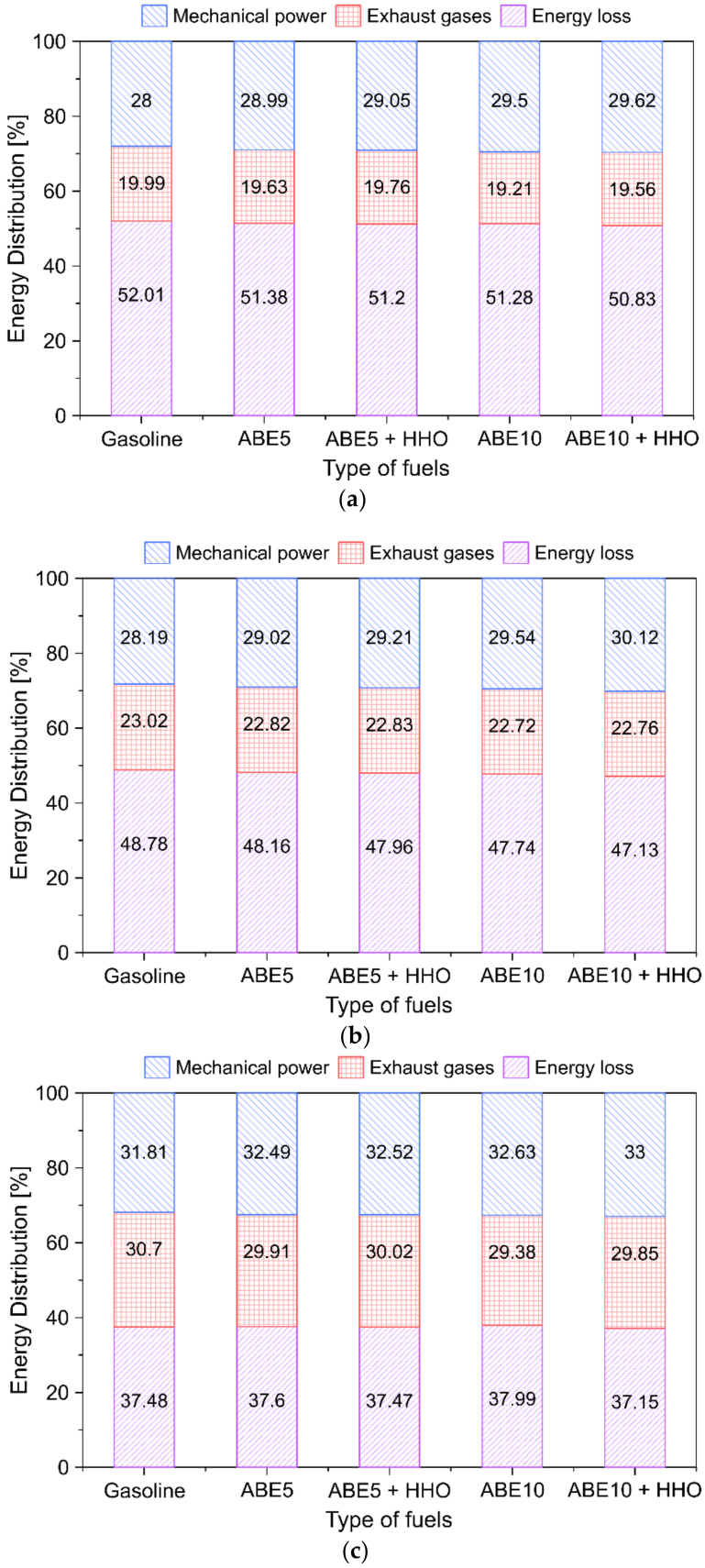

Figure 11. Energy distribution in the SI engine, (**a**) load 50%, (**b**) load 75% and (**c**) load 100%.

According to the results, increasing the engine load intensifies the energy contribution of both the power output and exhaust gases. This result is consistent with WHR applications where higher loads facilitate the fuel utilization ratio. The exhaust streams feature higher temperatures which corroborate the imminent escalation of NOx emission as depicted in Figure 9 [3,5]. However, the negative pattern of increasing the engine load is the significant rise in fuel consumption, as ratified in Figure 6. The results demonstrated that almost half of the fuel energy results in energy losses and other sources. Partial fuel substitution with ABE reduces the heat recovery potential from exhaust gases compared to conventional gasoline, which can be associated with the lower calorific value of this fuel blend.

Overall, ABE 10 + HHO features the best performance on the power output distribution from the tested fuels ranges in all the engine load conditions. An average increment of nearly 2.4% can be achieved compared to the baseline fuel. Contrarily, the maximum heat potential in the exhaust gases is higher in the gasoline fuel, with an improvement between 0.6–0.9% compared to the rest tested fuels. Subsequently, Figure 12 describes the behavior of thermal efficiency for the different fuel blends.

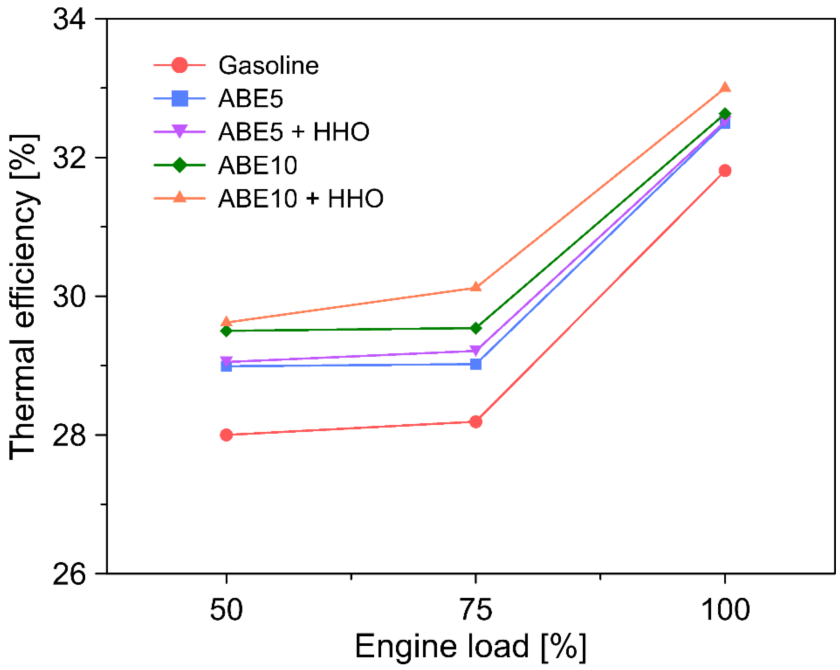

Figure 12. Thermal efficiency for different types of fuels.

According to the results, the thermodynamic efficiency directly relates to the engine load while representing a sensitivity between 4–6%. The latter can be attributed to non-optimized combustion derived from lower H_{RR} and pressure ranges. This pattern is consistent with similar applications in diesel engines operating in dual-fuel mode [15,16]. Moreover, the comparative assessment between fuel blends demonstrates that the addition of ABE in gasoline endorses engine efficiency, while hydroxy doping favors efficiency escalation. For the tested conditions, the maximum thermal efficiency of 31.81%, 32.49%, 32.52%, 32.63%, and 33.01% was obtained when operating with gasoline, ABE5, ABE5 + HHO, ABE10, and ABE10 + HHO, respectively. The above behavior is mainly attributed to a complete combustion process due to the presence of ABE and hydroxy, which is reflected in the reduction of CO emissions (see Figure 7).

Figure 13 shows the exergy distribution of the engine for the different operating conditions and fuel blends.

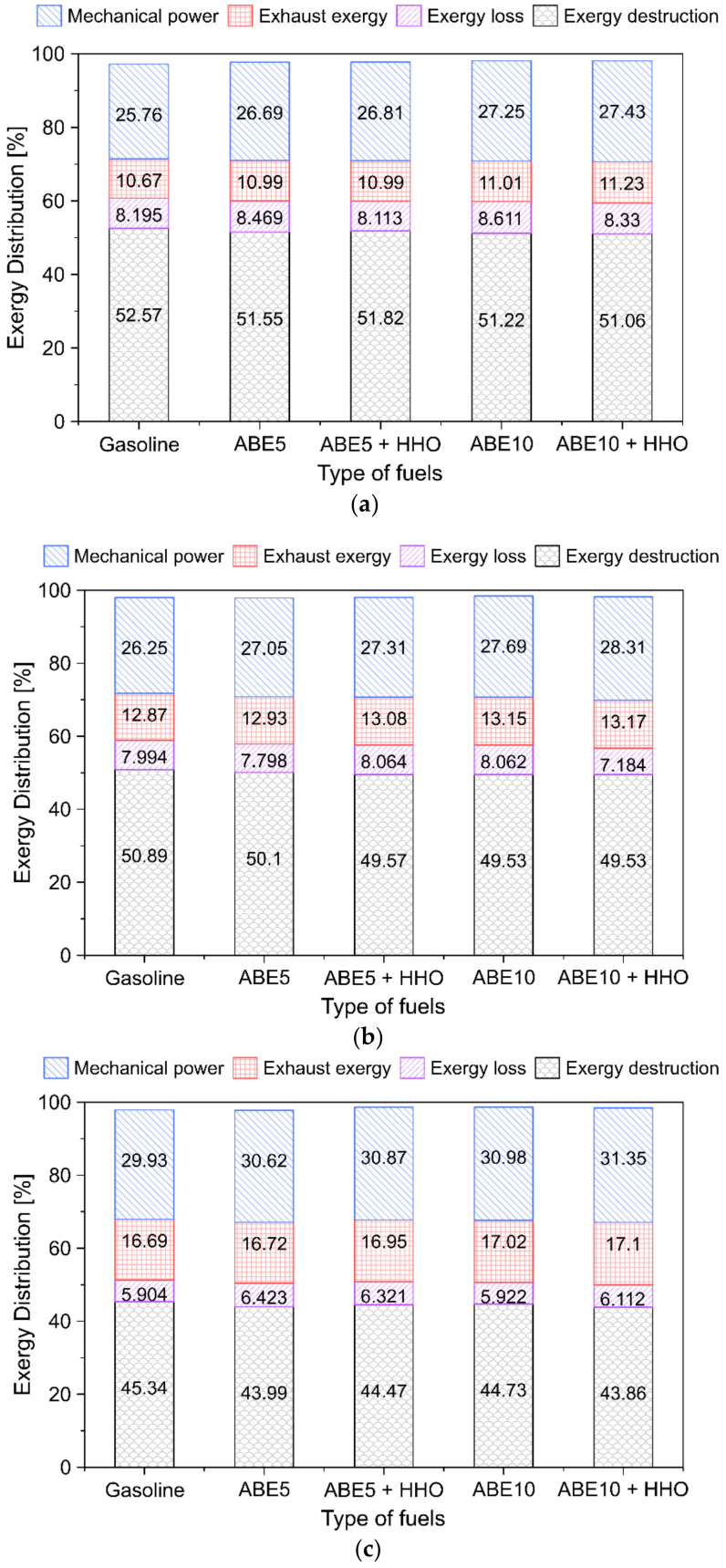

Figure 13. Exergy distribution in the SI engine, (**a**) load 50%, (**b**) load 75% and (**c**) load 100%.

Results show that exergy destruction represents the greatest share from the sources analyzed. The latter can be attributed to several factors such as residual fuel mixing, turbulence flow instabilities during combustion, among other irreversibilities that limit the chemical energy conversion [47]. Besides, as the engine load increases, both the useful exergy (mechanical power) and exhaust gas exergy rise, which implies improved combustion efficiency as both internal and external irreversibilities decrease [47,48]. The engine reaches a maximum of 29.9%, 30.6%, 30.9%, 31.0%, and 31.4% for the useful exergy when implementing gasoline fuels ABE5, ABE5 + HHO, ABE10, and ABE10 + HHO, respectively.

4. Conclusions

This investigation reports the potential application of dual-fuel operation in SI engines using acetone–butanol–ethanol (ABE) and hydroxy gas (HHO) enrichment. We characterized the main operation and design constraints of an experimental setup that combines a 3.5 kW YAMAHA engine and HHO generation. The evaluated fuel blends were ABE 5, ABE 5 + HHO, ABE 10, and ABE 10 + HHO, and gasoline was the baseline fuel. The core findings of the investigation can be summarized as follows:

- ABE standalone blends reduced both in-cylinder pressure and heat release rate compared to pure gasoline. Contrarily, hydroxy enrichment intensified the former and the latter while promoting a homogeneous fuel mixture.
- Engine load directly affected the combustion phasing leading to advanced or retarded combustion in the range of 0.2°–1.2°.
- ABE-based blends increase BSFC between 10–25 g • kWh^{-1} compared to pure gasoline due to lower calorific value and lower energy density. The partial fuel substitution with hydroxy gas counterbalanced this rise while obtaining a net BSFC reduction compared to the baseline fuel.
- The implementation of dual-fuel operation promoted a significant minimization of CO, HC, and smoke levels. However, CO_2 and NOx emissions escalated due to enhanced combustion oxidation and higher combustion temperatures, which opens a new path for incorporating advanced fuel injection systems and after-exhaust treatment technologies.
- Energy losses represented a predominant share (37–52%) from the chemical energy input depending on the load. Increasing ABE and HHO content in the dual-fuel operation maximizes the power output by up to 2.2%. In contrast, high-load conditions promoted the minimization of energy losses, which implies higher combustion efficiency.
- ABE 10 + HHO featured the highest thermal efficiency (28–33%) from the fuel blends. Moreover, hydroxy doping increased efficiency up to 1.8%.
- Exergy destruction represents up to half of the exergy distribution, demonstrating the predominant share of internal irreversibilities in the combustion phenomena. Dual-fuel mode and higher engine loads result in enhanced useful exergy and power output.

The implementation of dual-fuel operation in SI engines demonstrated promising results towards emissions reduction and enhanced combustion performance. Further studies should assess the effect of engine speed on engine performance and control of the spark timing. Emissions maps are a robust tool to predict emissions levels and thermal performance. The incorporation of advanced technologies such as control strategies, waste heat recovery, and exhaust gas recirculation stand as promising avenues in the long-term perspectives of ICEs to further enhance the fuel utilization ratio.

Author Contributions: Conceptualization, W.G.-E., D.M.-C. and J.D.-F.; Methodology, W.G.-E., D.M.-C., A.B.-S. and J.D.-F.; Software, W.G.-E., D.M.-C., A.G.-Q. and J.D.-F.; Validation, A.B.-S., A.G.-Q. and J.D.-F.; Formal Analysis, W.G.-E. and D.M.-C.; Investigation, W.G.-E. and D.M.-C.; Resources, A.B.-S., A.G.-Q. and J.D.-F.; Writing—Original Draft Preparation, W.G.-E., D.M.-C. and A.G.-Q.; Writing—Review and Editing, A.B.-S. and J.D.-F.; Funding Acquisition, W.G.-E. and A.B.-S. All authors have read and agreed to the published version of the manuscript.

Funding: This research received no external funding.

Institutional Review Board Statement: Not applicable.

Informed Consent Statement: Not applicable.

Data Availability Statement: Not applicable.

Acknowledgments: Acknowledgments to Universidad del Atlántico through the project ING81-CII2019 "Estudio experimental de la sustitución parcial de combustible con HIDROXY (HHO) en motores térmicos de encendido por compresión y la influencia sobre sus prestaciones", Universidad del Norte, Sphere Energy Company for the support provided for the investigative internship of Daniel Maestre, and Colombian Institute for Scientific and Technological Development (COLCIENCIAS) through the "Convocatoria 809 Minciencias, Formación de capital humano de alto nivel para las regiones- Atlántico" for the support provided.

Conflicts of Interest: The authors declare no conflict of interest.

Abbreviations

The following abbreviations are used in this manuscript:

ABE	Acetone–Butanol–Ethanol
BSFC	Break specific fuel consumption
CI	Compression ignition
HHO	Hydroxy gas
LHV	Lower heating value
ICE	Internal combustion engine
H_{RR}	Heat release rate
SI	Spark ignition
BSFC	Brake specific fuel consumption
CO	Carbon monoxide
CO2	Carbon dioxide
NOx	Nitrogen oxides
HC	Hydrocarbons
WHR	Waste heat recovery
Nomenclature	
A	Area
b	Internal diameter of the combustion chamber
b_i	Best estimate of measurement
P	Mean combustion chamber pressure
V	Combustion chamber volume
m	Gas mass
k_{dry}/k_{wet}	Empirical emission gas constants
k_1/k_2	Model constants
k_{def}	Deformation constant
C_v/C_p	Specific heat at constant volume/pressure
T	Combustion chamber gas temperature
Q	Heat release
Q_r	Heat rejected by convection
H	Enthalpy
h	Specific enthalpy
h_{wall}	Heat transfer coefficient of the wall
R	Ideal gas constant
N	Engine speed
n	Number of repetitions
PW	Power output
R_y	Vertical position of the piston
S_t	Engine stroke
S	Standard deviation
T_r	Engine torque

U	Internal energy
u	Specific Internal Energy
X	Gas Mass Fraction
A_{wall}	Heat transfer surface area of the combustion chamber
A_c	Connecting rod's critical area
D	Diameter
L	Length
EP	Pollutant emissions in power unit
EV	Exhaust emissions in ppm/%vol.
r_c	Compression ratio
E_s	Elastic modulus of steel
a_p	Piston acceleration
e	Eccentricity between the stump and the bearing, located in its centerline
M	Gas molecular weight
W	Mechanical work
w	Average velocity of the combustion chamber
x_i	Measurement
Greek Letters	
θ	Crankshaft angle
Δ	Differential variation
ρ	Fluid density
α	Angle between the connecting rod and piston
φ	Rotational angle
γ	Specific heat ratio
ω	Angular speed
η	Efficiency
Subscripts	
0	Initial conditions
comb	Combustion chamber gas
bb	Blow-by gas
cr	Crankshaft
D	Discharge
dp	Pressure deformation
disp	Displaced
ext	Exhaust
st	Stoichiometric combustion
m	Mean
mech	Mechanical
mv	Top-dead center volume
t	Theoretical
g	Gaseous fuel
v	Valve
int	Intake/inlet
inf	Inertial forces

References

1. Matrisciano, A.; Franken, T.; Mestre, L.C.G.; Borg, A.; Mauss, F. Development of a Computationally Efficient Tabulated Chemistry Solver for Internal Combustion Engine Optimization Using Stochastic Reactor Models. *Appl. Sci.* **2020**, *10*, 8979. [CrossRef]
2. Ochoa, G.V.; Rojas, J.P.; Forero, J.D. Advance Exergo-Economic Analysis of a Waste Heat Recovery System Using ORC for a Bottoming Natural Gas Engine. *Energies* **2020**, *13*, 267. [CrossRef]
3. Ochoa, G.V.; Gutierrez, J.C.; Forero, J.D. Exergy, Economic, and Life-Cycle Assessment of ORC System for Waste Heat Recovery in a Natural Gas Internal Combustion Engine. *Resources* **2020**, *9*, 2. [CrossRef]
4. Forero, J.D.; Taborda, L.L.; Silvera, A.B. Characterization of the performance of centrifugal pumps powered by a diesel engine in dredging applications. *Int. Rev. Mech. Eng. (IREME)* **2019**, *13*, 11–20. [CrossRef]
5. Valencia, G.; Duarte, J.; Isaza-Roldan, C. Thermoeconomic Analysis of Different Exhaust Waste-Heat Recovery Systems for Natural Gas Engine Based on ORC. *Appl. Sci.* **2019**, *9*, 4017. [CrossRef]
6. Diaz, G.A.; Forero, J.D.; Garcia, J.; Rincon, A.; Fontalvo, A.; Bula, A.J.; Padilla, R.V. Maximum Power From Fluid Flow by Applying the First and Second Laws of Thermodynamics. *J. Energy Resour. Technol.* **2017**, *139*, 032903. [CrossRef]

7. Ochoa, G.V.; Isaza-Roldan, C.; Forero, J.D. Economic and Exergo-Advance Analysis of a Waste Heat Recovery System Based on Regenerative Organic Rankine Cycle under Organic Fluids with Low Global Warming Potential. *Energies* **2020**, *13*, 1317. [CrossRef]
8. Orozco, W.; Acuña, N.; Duarte, J. Characterization of Emissions in Low Displacement Diesel Engines Using Biodiesel and Energy Recovery System. *Int. Rev. Mech. Eng. (IREME)* **2019**, *13*, 420–426. [CrossRef]
9. Tamilselvan, P.; Nallusamy, N.; Rajkumar, S. A comprehensive review on performance, combustion and emission characteristics of biodiesel fuelled diesel engines. *Renew. Sustain. Energy Rev.* **2017**, *79*, 1134–1159. [CrossRef]
10. Masum, B.M.; Kalam, M.A.; Masjuki, H.H.; Palash, S.M.; Fattah, I.M.R. Performance and emission analysis of a multi cylinder gasoline engine operating at different alcohol–gasoline blends. *RSC Adv.* **2014**, *4*, 27898–27904. [CrossRef]
11. Yacoub, Y.M.; Bata, R.M.; Gautam, M. The performance and emission characteristics of C1-C5 alcohol-gasoline blends with matched oxygen content in a single-cylinder spark ignition engine. *Proc. Inst. Mech. Eng. Part A J. Power Energy* **1998**, *212*, 363–379. [CrossRef]
12. Nithyanandan, K.; Zhang, J.; Li, Y.; Wu, H.; Lee, T.H.; Lin, Y.; Lee, C.-F.F. Improved SI engine efficiency using Acetone–Butanol–Ethanol (ABE). *Fuel* **2016**, *174*, 333–343. [CrossRef]
13. Di Blasio, G.; Viscardi, M.; Alfè, M.; Gargiulo, V.; Ciajolo, A.; Beatrice, C. Analysis of the Impact of the Dual-Fuel Ethanol-Diesel System on the Size, Morphology, and Chemical Characteristics of the Soot Particles Emitted from a LD Diesel Engine. *SAE Tech. Pap. Ser.* **2014**. [CrossRef]
14. Gargiulo, V.; Alfe, M.; Di Blasio, G.; Beatrice, C. Chemico-physical features of soot emitted from a dual-fuel ethanol–diesel system. *Fuel* **2015**, *150*, 154–161. [CrossRef]
15. Beatrice, C.; Denbratt, I.; Di Blasio, G.; Di Luca, G.; Ianniello, R.; Saccullo, M. Experimental Assessment on Exploiting Low Carbon Ethanol Fuel in a Light-Duty Dual-Fuel Compression Ignition Engine. *Appl. Sci.* **2020**, *10*, 7182. [CrossRef]
16. Vassallo, A.; Beatrice, C.; Di Blasio, G.; Belgiorno, G.; Avolio, G.; Pesce, F.C. The Key Role of Advanced, Flexible Fuel Injection Systems to Match the Future CO_2 Targets in an Ultra-Light Mid-Size Diesel Engine. *SAE Tech. Pap. Ser.* **2018**. [CrossRef]
17. Belgiorno, G.; Dimitrakopoulos, N.; Di Blasio, G.; Beatrice, C.; Tunestål, P.; Tunér, M. Effect of the engine calibration parameters on gasoline partially premixed combustion performance and emissions compared to conventional diesel combustion in a light-duty Euro 6 engine. *Appl. Energy* **2018**, *228*, 2221–2234. [CrossRef]
18. Milani, D.; Kiani, A.; McNaughton, R. Renewable-powered hydrogen economy from Australia's perspective. *Int. J. Hydrogen Energy* **2020**, *45*, 24125–24145. [CrossRef]
19. Escobar-Yonoff, R.; Maestre-Cambronel, D.; Charry, S.; Rincón-Montenegro, A.; Portnoy, I. Performance assessment and economic perspectives of integrated PEM fuel cell and PEM electrolyzer for electric power generation. *Heliyon* **2021**, *7*, e06506. [CrossRef]
20. Alshehri, F.; Suárez, V.G.; Torres, J.L.R.; Perilla, A.; van der Meijden, M. Modelling and evaluation of PEM hydrogen technologies for frequency ancillary services in future multi-energy sustainable power systems. *Heliyon* **2019**, *5*, e01396. [CrossRef]
21. Shivaprasad, K.; Raviteja, S.; Chitragar, P.; Kumar, G. Experimental Investigation of the Effect of Hydrogen Addition on Combustion Performance and Emissions Characteristics of a Spark Ignition High Speed Gasoline Engine. *Procedia Technol.* **2014**, *14*, 141–148. [CrossRef]
22. Ismail, T.M.; Ramzy, K.; Elnaghi, B.E.; Mansour, T.; Abelwhab, M.; El-Salam, M.A.; Ismail, M. Modelling and simulation of electrochemical analysis of hybrid spark-ignition engine using hydroxy (HHO) dry cell. *Energy Convers. Manag.* **2019**, *181*, 1–14. [CrossRef]
23. Yilmaz, A.C.; Uludamar, E.; Aydin, K. Effect of hydroxy (HHO) gas addition on performance and exhaust emissions in compression ignition engines. *Int. J. Hydrogen Energy* **2010**, *35*, 11366–11372. [CrossRef]
24. Carl, J.; Fedor, D. Tracking global carbon revenues: A survey of carbon taxes versus cap-and-trade in the real world. *Energy Policy* **2016**, *96*, 50–77. [CrossRef]
25. Mendoza-Casseres, D.; Valencia-Ochoa, G.; Duarte-Forero, J. Experimental assessment of combustion performance in low-displacement stationary engines operating with biodiesel blends and hydroxy. *Therm. Sci. Eng. Prog.* **2021**, *23*, 100883. [CrossRef]
26. Dhinesh, B.; Raj, Y.M.A.; Kalaiselvan, C.; KrishnaMoorthy, R. A numerical and experimental assessment of a coated diesel engine powered by high-performance nano biofuel. *Energy Convers. Manag.* **2018**, *171*, 815–824. [CrossRef]
27. van Wyk, S.; van der Ham, A.; Kersten, S. Pervaporative separation and intensification of downstream recovery of acetone-butanol-ethanol (ABE). *Chem. Eng. Process. Process. Intensif.* **2018**, *130*, 148–159. [CrossRef]
28. Anderhofstadt, B.; Spinler, S. Preferences for autonomous and alternative fuel-powered heavy-duty trucks in Germany. *Transp. Res. Part D Transp. Environ.* **2020**, *79*, 102232. [CrossRef]
29. Ismail, T.M.; Ramzy, K.; Abelwhab, M.; Elnaghi, B.E.; El-Salam, M.A.; Ismail, M. Performance of hybrid compression ignition engine using hydroxy (HHO) from dry cell. *Energy Convers. Manag.* **2018**, *155*, 287–300. [CrossRef]
30. Ferguson, C.R.; Kirkpatrick, A.T. *Internal Combustion Engines—Applied Thermosciences*; John Wiley & Sons: Hoboken, NJ, USA, 2001.
31. Williams, F.A. *Combustion Theory Benjamin/Cummings*; Westview Press: Menlo Park, CA, USA, 1985.
32. Ochoa, G.V.; Isaza-Roldan, C.; Forero, J.D. A phenomenological base semi-physical thermodynamic model for the cylinder and exhaust manifold of a natural gas 2-megawatt four-stroke internal combustion engine. *Heliyon* **2019**, *5*, e02700. [CrossRef]
33. Pain, J. Gas Dynamics. *Nat. Cell Biol.* **1967**, *213*, 1182. [CrossRef]

34. Hernández-Comas, B.; Maestre-Cambronel, D.; Pardo-García, C.; Fonseca-Vigoya, M.; Pabón-León, J. Influence of Compression Rings on the Dynamic Characteristics and Sealing Capacity of the Combustion Chamber in Diesel Engines. *Lubricants* **2021**, *9*, 25. [CrossRef]
35. Irimescu, A.; Di Iorio, S.; Merola, S.S.; Sementa, P.; Vaglieco, B.M. Evaluation of compression ratio and blow-by rates for spark ignition engines based on in-cylinder pressure trace analysis. *Energy Convers. Manag.* **2018**, *162*, 98–108. [CrossRef]
36. Woschni, G. A Universally Applicable Equation for the Instantaneous Heat Transfer Coefficient in the Internal Combustion Engine. *SAE Tech. Pap. Ser.* **1967**. [CrossRef]
37. Consuegra, F.; Bula, A.; Guillín, W.; Sánchez, J.; Forero, J.D. Instantaneous in-Cylinder Volume Considering Deformation and Clearance due to Lubricating Film in Reciprocating Internal Combustion Engines. *Energies* **2019**, *12*, 1437. [CrossRef]
38. Ağbulut, Ü.; Sarıdemir, S.; Albayrak, S. Experimental investigation of combustion, performance and emission characteristics of a diesel engine fuelled with diesel–biodiesel–alcohol blends. *J. Braz. Soc. Mech. Sci. Eng.* **2019**, *41*, 389. [CrossRef]
39. Heseding, M.; Daskalopoulos, P. *Exhaust Emission Legislation-Diesel-and Gas Engines*; VDMA: Frankfurt Am Main, Germany, 2006.
40. Musthafa, M.M.; Kumar, T.A.; Mohanraj, T.; Chandramouli, R. A comparative study on performance, combustion and emission characteristics of diesel engine fuelled by biodiesel blends with and without an additive. *Fuel* **2018**, *225*, 343–348. [CrossRef]
41. Ma, F.; Wang, M.; Jiang, L.; Deng, J.; Chen, R.; Naeve, N.; Zhao, S. Performance and emission characteristics of a turbocharged spark-ignition hydrogen-enriched compressed natural gas engine under wide open throttle operating conditions. *Int. J. Hydrogen Energy* **2010**, *35*, 12502–12509. [CrossRef]
42. Senthilkumar, S.; Sivakumar, G.; Manoharan, S. Investigation of palm methyl-ester bio-diesel with additive on performance and emission characteristics of a diesel engine under 8-mode testing cycle. *Alex. Eng. J.* **2015**, *54*, 423–428. [CrossRef]
43. Zhang, J.; Nithyanandan, K.; Li, Y.; Lee, C.-F.; Huang, Z. Comparative Study of High-Alcohol-Content Gasoline Blends in an SI Engine. *SAE Tech. Pap. Ser.* **2015**, *1*. [CrossRef]
44. Duarte, J.; Amador, G.; Garcia, J.; Fontalvo, A.; Padilla, R.V.; Sanjuan, M.; Quiroga, A.G. Auto-ignition control in turbocharged internal combustion engines operating with gaseous fuels. *Energy* **2014**, *71*, 137–147. [CrossRef]
45. Duarte, J.; Garcia, J.; Jiménez, J.; Sanjuan, M.E.; Bula, A.; González, J. Auto-Ignition Control in Spark-Ignition Engines Using Internal Model Control Structure. *J. Energy Resour. Technol.* **2017**, *139*, 022201. [CrossRef]
46. Li, Y.; Nithyanandan, K.; Zhang, J.; Lee, C.-F.; Liao, S. Combustion and Emissions Performance of a Spark Ignition Engine Fueled with Water Containing Acetone-Butanol-Ethanol and Gasoline Blends. *SAE Tech. Pap. Ser.* **2015**. [CrossRef]
47. Kul, B.S.; Kahraman, A. Energy and Exergy Analyses of a Diesel Engine Fuelled with Biodiesel-Diesel Blends Containing 5% Bioethanol. *Entropy* **2016**, *18*, 387. [CrossRef]
48. Monsalve-Serrano, J.; Belgiorno, G.; Di Blasio, G.; Guzmán-Mendoza, M. 1D Simulation and Experimental Analysis on the Effects of the Injection Parameters in Methane–Diesel Dual-Fuel Combustion. *Energies* **2020**, *13*, 3734. [CrossRef]